Edifice strength and magma transfer modulation at Piton de la Fournaise volcano

Jean-Luc Got, Aline Peltier, Thomas Staudacher, Philippe Kowalski, Patrice Boissier

JOURNAL OF GEOPHYSICAL RESEARCH: SOLID EARTH, VOL. 118, 5040–5057, doi:10.1002/jgrb.50350, 2013

Edifice strength and magma transfer modulation at Piton de la Fournaise volcano

Jean-Luc Got,[1] Aline Peltier,[2] Thomas Staudacher,[3] Philippe Kowalski,[3] and Patrice Boissier[3]

Received 6 May 2013; revised 18 July 2013; accepted 20 August 2013; published 12 September 2013.

[1] From 2003 to 2007, eruptive activity at Piton de la Fournaise was shown to follow cycles, comprising many summit/proximal eruptions and finishing by a distal eruption. GPS measurements evidenced striking asymmetric deformation between its western and eastern flanks. Horizontal displacements recorded during interdistal periods showed a characteristic amplitude at the top of the eastern flank. Displacements recorded at the base of the summit cone showed a bimodal distribution, with low amplitudes during interdistal periods and large ones during distal eruptions. To account for displacement asymmetry, characteristic amplitude, and large flank displacement, we modeled the volcanic edifice using a Drücker-Prager elastoplastic rheology. Friction angles of 15° and >30° were needed to model the displacements respectively during distal eruptions and interdistal periods; this change shows that strain weakening occurred during distal events. Large plastic displacement that occurred in the eastern flank during distal eruptions relaxed the horizontal elastic stress accumulated during interdistal periods; it triggered summit deflation, horizontal magma transfer, and distal flank eruption and reset the eruptive cycle. Our elastoplastic models also show that simple source geometries may induce large eastern flank displacements that would be explained by a complex geometry in a linear elastic edifice. Magma supply is often thought to control volcano's eruptive activity, with surface deformation reflecting changes in magma supply rate, the volcano's response being linear. Our results bring some evidences that on Piton de la Fournaise time-space discretization of magma transfer may be the result of the edifice's nonlinear response, rather than changes in magma supply.

Citation: Got, J.-L., A. Peltier, T. Staudacher, P. Kowalski, and P. Boissier (2013), Edifice strength and magma transfer modulation at Piton de la Fournaise volcano, *J. Geophys. Res. Solid Earth*, *118*, 5040–5057, doi:10.1002/jgrb.50350.

1. Introduction

[2] Magma flux through volcanoes to the Earth's surface is discontinuous, whereas the deep heat flux is continuous and may be considered constant over the time scales corresponding to large numbers of volcanic eruptions [e.g., *Vidal and Bonneville*, 2004]. At Kilauea volcano, Hawaii, *Poland et al.* [2012] recently showed that the mantle magma supply rate remained constant from 1952 to 2002 and interpreted the 2002–2007 inflation as a high-frequency variation in the magma supply rate. However, evidencing magma supply rate variations from mantle is still a matter of debate.

[3] Large basaltic volcanoes, such as Hawaiian volcanoes, Etna, and the Piton de la Fournaise, often have characteristic structures, showing large deformation such as rift zones and asymmetrical displacements with more or less mobile flanks, which indicate long-lasting stress field conditions. Hawaiian volcanoes share complex topographic features, which evidence the reproducibility of a complex deformation pattern, though conditions of magma supply and contact with the oceanic crust are similar and simple. Rift zones at Kilauea volcano are well developed and flank displacement rates average several centimeters per year [*Swanson et al.*, 1976; *Owen et al.*, 1995] producing periodic slow slip events [*Cervelli et al.*, 2002; *Segall et al.*, 2006; *Brooks et al.*, 2006, 2008] and large magnitude earthquakes. Kilauea volcano has been in continuous eruption since 1 January 1983 with deflation of the summit from 1983 to 2002. In contrast, Etna and the Piton de la Fournaise, which have less well-developed rift zones and less mobile flanks, only produce discrete eruptions that may be grouped into cycles [*Behncke and Neri*, 2003; *Allard et al.*, 2006; *Peltier et al.*, 2008, 2009a]. Although basaltic volcanoes share some characteristics, especially in terms of magma supply, composition, viscosity, and morphology of the edifice, they often have different eruptive dynamics. Are these various eruptive dynamics caused by mantle processes or by more superficial processes? In this paper, we present rare observational evidences at Piton de la Fournaise that may help understanding

[1]ISTerre, CNRS, Université de Savoie, Le Bourget-du-Lac, France.
[2]Institut de Physique du Globe de Paris et Université Paris Diderot (Sorbonne Paris-Cité), Paris, France.
[3]Observatoire Volcanologique du Piton de la Fournaise, IPGP, UMR CNRS, La Plaine des Cafres, France.

Corresponding author: J.-L. Got, ISTerre, CNRS, Université de Savoie, Le Bourget-du-Lac FR-73376, France. (jlgot@univ-savoie.fr)

2169-9313/13/10.1002/jgrb.50350

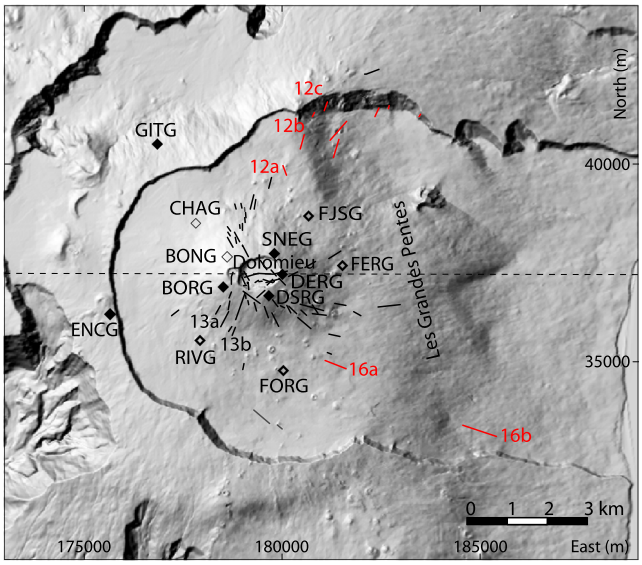

Figure 1. Map of the Piton de la Fournaise volcano showing the OVPF permanent GPS network (diamonds) and the eruptive fissures (lines) for the period 1998–2007. Red and black lines indicate the location of eruptive fissures associated with distal and summit/proximal eruptions, respectively. The numbers refer to the studied eruptions (Table 1). Summit GPS stations (installed in 2004; full black diamonds), basal GPS stations (installed in August 2005; thick diamonds), and GPS stations installed in January 2007 (thin diamonds). The dashed line corresponds to the cross section presented in Figures 10–14. The eastern flank is the area located east of the summit cone and extending up to the sea. In the text, "upper eastern flank" refers to the region around FERG-FJSG. Coordinates are given in the Gauss-Laborde Réunion projection system.

these processes and the relationship that may exist between eventual eruptive cycles, stress, strain, edifice strength, and surface displacement asymmetry in basaltic volcanoes.

[4] Piton de la Fournaise, a hot spot shield volcano on La Réunion Island, Indian Ocean, erupted 34 times between 9 March 1998 and 10 December 2010, emitting ~500 × 10^6 m^3 of magma to the surface [*Roult et al*., 2012]. These eruptions were of three types and succeeded one another following eruptive cycles [*Peltier et al*., 2009a]: (1) the two most common types (89% of eruptions) were summit and proximal eruptions with eruptive fissures within a 2 km radius of the summit crater. (2) The third type that ended a cycle was large flank or distal eruptions (five during this period), with eruptive fissures that opened at low elevation, at distances greater than 4 km from the summit crater (Figure 1). Displacements measured at the surface, and volumes of lava emitted during distal eruptions are the largest (mean volumes of 20 × 10^6 m^3 against 4 × 10^6 m^3 and 2 × 10^6 m^3 for the proximal and summit eruptions, respectively) and their compositions are olivine rich (>20% vol.) [e.g., *Famin et al*., 2009; *Peltier et al*., 2009a]. The current view of the shallow magma feeding system consists of a shallow ellipsoidal reservoir, located below the Dolomieu crater at an altitude of 0–500 m above sea level (that is, about 2000 m below the summit), from which the dykes root; it was inferred from seismic tomography [*Nercessian et al*., 1996; *Prono et al*., 2009] or by inversion of geodetic data [*Peltier et al*., 2007, 2008, 2009b]. The edifice is thought to be composed by a western flank, considered as stable, and an eastern flank displaced during some eruptions [see, e.g., *Peltier et al*., 2007, 2009a]; these flanks are separated by a rift system [*Bachèlery*, 1981; *Michon et al*., 2007a; *Bonali et al*., 2010]. Geological direct surface observations and statistics [e.g., *Bachèlery*, 1981; *Letourneur et al*., 2008; *Peltier et al*., 2012] mostly show subvertical dykes, whereas elastic inversion of geodetic data leads to large residuals in the eastern or western flank, or to eastward dipping dykes [*Fukushima et al*., 2005; *Peltier et al*., 2007].

[5] Eruptive cycles and distal eruptions, occurrence of rifting, asymmetry, and timing of the displacements may be investigated in terms of stress, strain, and edifice strength by studying the magma-edifice interaction. In this paper, we study more specifically the effect of rock rheology and strength (reaction when loaded) on the dynamics of volcanic processes at Piton de la Fournaise, exploring beyond linear elasticity, which is mostly used when modeling surface deformation. From this study, we propose a synthetic and unifying explanation for both the asymmetry and timing of the deformation, the eruptive and stress cycles, the occurrence of distal eruptions, and finally the magma transfer from the mantle to the surface at Piton de la Fournaise.

2. GPS Data and Processing

[6] The OVPF (Observatoire Volcanologique du Piton de la Fournaise) set up a permanent GPS network on Piton de la Fournaise in 2004 and 2005, installing summit stations in 2004 and basal stations in August–September 2005 (Figure 1). GPS signals are recorded at a rate of 2 samples/min. We used Ashtech Solution software to determine positions (GITG station being the reference station) at the same rate. Mean horizontal and vertical accuracies were ~0.5 and ~2.5 cm, respectively. We also calculated daily means. To complete the permanent GPS network, a dense network of 80 stainless steel benchmarks was implemented around the summit cone to its base. Benchmark positions were measured in rapid-static mode immediately after each eruption, since 2003, with an acquisition time of 7 min at a period of 1 measurement per second. The accuracy of these rapid-static mode data was 1–2 cm horizontally and 2–3 cm vertically. Our study mostly focused on the period 2003–2007, which preceded the large summit collapse event and major eruption (240 Mm^3 magma released) [*Roult et al*., 2012] of April 2007 (see *Michon et al*. [2007b], *Peltier et al*. [2009b], and *Staudacher et al*. [2009] for more detail on this well-documented eruption). Eleven summit/proximal and four distal eruptions were recorded during this period (Table 1).

[7] Because the 30 March 2007 deformation process was complex (Figure 2b), especially at its onset, we performed a thorough analysis of the corresponding GPS signal. In order to assess the probability that a GPS position measurement would actually be within a given interval, we carefully investigated the properties of the noise on these measurements. We computed probability density functions for the hour preceding the 30 March 2007 16:30 substantial displacement for various GPS stations (Figure 3). However, noise on GPS position measurements is nonstationary and depends on external causes, mostly atmospheric or stratospheric. It is therefore necessary to investigate noise as a function of frequency (or period) in order to determine the order of magnitude of the short-period and long-period components of the noise.

Table 1. Eruptions Occurring Since the First Measurements of the OVPF Reiterated GPS Network From *Roult et al*. [2012][a]

Number	Start of Events	End of Events	Type	Direction	Location
1	30/05/03	07/07/03	S		Dolomieu
2	22/08/03	27/08/03	P	17	N flank
3	30/09/03	01/10/03	P	203	SW flank
4	06/11/03	06/11/06	I	144	SE-E flank
5	07/12/03	25/12/03	S	37	Dolomieu
6	08/01/04	10/01/07	D	24	NE flank
7	02/05/04	18/05/04	P	191	S flank
8	12/08/04	14/10/04	SP	71	Dolomieu + E flank
9	17/02/05	26/02/05	D	30	NE flank
10	04/10/05	17/10/05	S	342	Dolomieu
11	29/11/05	29/11/05	SP	358	N flank
12	26/12/05	18/01/06	D	35	NE flank
13	20/07/06	14/08/06	P	202	S flank
14	30/08/06	31/12/06	S	77	Dolomieu
15	18/02/07	19/02/07	SP	90	Dolomieu + E flank
16	30/03/07	01/05/07	D	118–125	SE flank
17	08/09/08	04/02/09	3S + 3I		Dolomieu
18	07/10/09	14/10/09	2I		
19	05/11/09	06/11/09	P	71	S-SE flank
20	14/12/09	15/12/09	P	118	S-SW flank
21	02/01/10	12/01/10	S	5	Dolomieu
22	14/10/10	31/10/10	P	164	S flank
23	09/12/10	10/12/10	P	−15	N flank

[a]Date is in day/month/year format; type is S for summit eruption, P for proximal eruption, D for distal eruption, and I for intrusion. Eruption beginning in the summit caldera and continuing by an eruptive fissure outside the caldera is labeled SP. Direction and location are the azimuth (deg) and location of the eruptive fissures. Simplified from *Roult et al*. [2012]; eruptions of 30 March and 2 April 2007 are gathered in only one event (30 March 2007), and the eruptive activity at the end of 2008 is gathered in three summit eruptions and three intrusions; eruptive activity of October 2009 is gathered in two intrusions.

Because ground displacements generated by magma injections at depth are relatively high-frequency signals, detection of such displacement is mainly controlled by the short-period noise. Consequently, we paid particular attention to the short-period components in the GPS measurement noise.

2.1. Noise Periodogram

[8] The spectral representation of the noise shows that noise amplitude strongly depends on the period. We computed the periodogram of the noise recorded during the hour preceding the strong vertical displacement measured by the FERG GPS station on 30 March at 16:30 (Figure 4). The periodogram showed that noise amplitude was less than 1 cm in the 0–10 min short-period band; it was stronger at longer periods. Over the long term, long-period components dominate the noise spectral amplitude but should not be confused with the short-period components involved in the short-period signal detection.

2.2. Transfer Function

[9] Because the noise affecting GPS position measurements is nonstationary, it is best to estimate it when a signal occurs. At the Piton de la Fournaise volcano, the GITG GPS station is located outside the Enclos Fouqué caldera (Figure 1), on the stable part of the volcano. Displacements measured at GITG are generally below the detection threshold, so GITG was used as the local reference station. It can also be used to estimate noise at the time the signal of interest occurs at other sites. Noise in GPS displacement data is actually more or less correlated between channels. This correlation allows a simple method, based on cross-spectral analysis, to be used to estimate noise during the period of interest. We used the 30 March 2007 records to first compute the transfer function of the filter relating the GITG and FERG GPS displacement signals during the hour preceding the signal (from 15:30 to 16:30; Figures A1a and A1b). This transfer function was computed as the ratio of the smoothed cross spectrum of those records to the smoothed autospectrum of the GITG record. We then applied this transfer function to the GITG displacement signal recorded between 16:30 and 17:30 in order to estimate the noise power for the FERG displacement data. Noise spectral amplitudes at GITG were stationary from 15:30 to 17:30. Our results (Figures A1c and A1d) show that the estimated noise amplitude between 16:30 and 17:30 at FERG vertical statistically corresponded to the second order variation recorded on the FERG vertical component between 16:30 and 17:30 (Figure 3b) and gave a reasonable estimate of the noise power during that time interval.

2.3. Determination of Cutoff Periods for Filtering

[10] Signals have to be filtered with cutoff frequencies chosen from the noise spectrum estimation. To determine cutoff periods, we used the noise samples recorded during the hour before the displacement signal preceding the beginning of the 30 March eruption. Noise-dominant periods were about 10–15 min during this time interval (Figure A1). We also estimated the noise superimposed on the displacement signal by computing the transfer function between the vertical component of the GITG reference station and of FERG for the same time period. The noise at FERG estimated by this method (Figure A1) shows a dominant period of about 10 min. The signal had a dominant period of about 1 h, so the noise and signal spectra overlapped. As a result, we used a bias-variance compromise strategy to choose the cutoff period: The cutoff period should not be too high, so it did not bias the signal, but it had to be sufficiently high to reduce the variance due to the noise. This strategy gave cutoff periods of 12 min for the FERG vertical component, 10 min for the FERG horizontal components, and 5 min for the DERG vertical component.

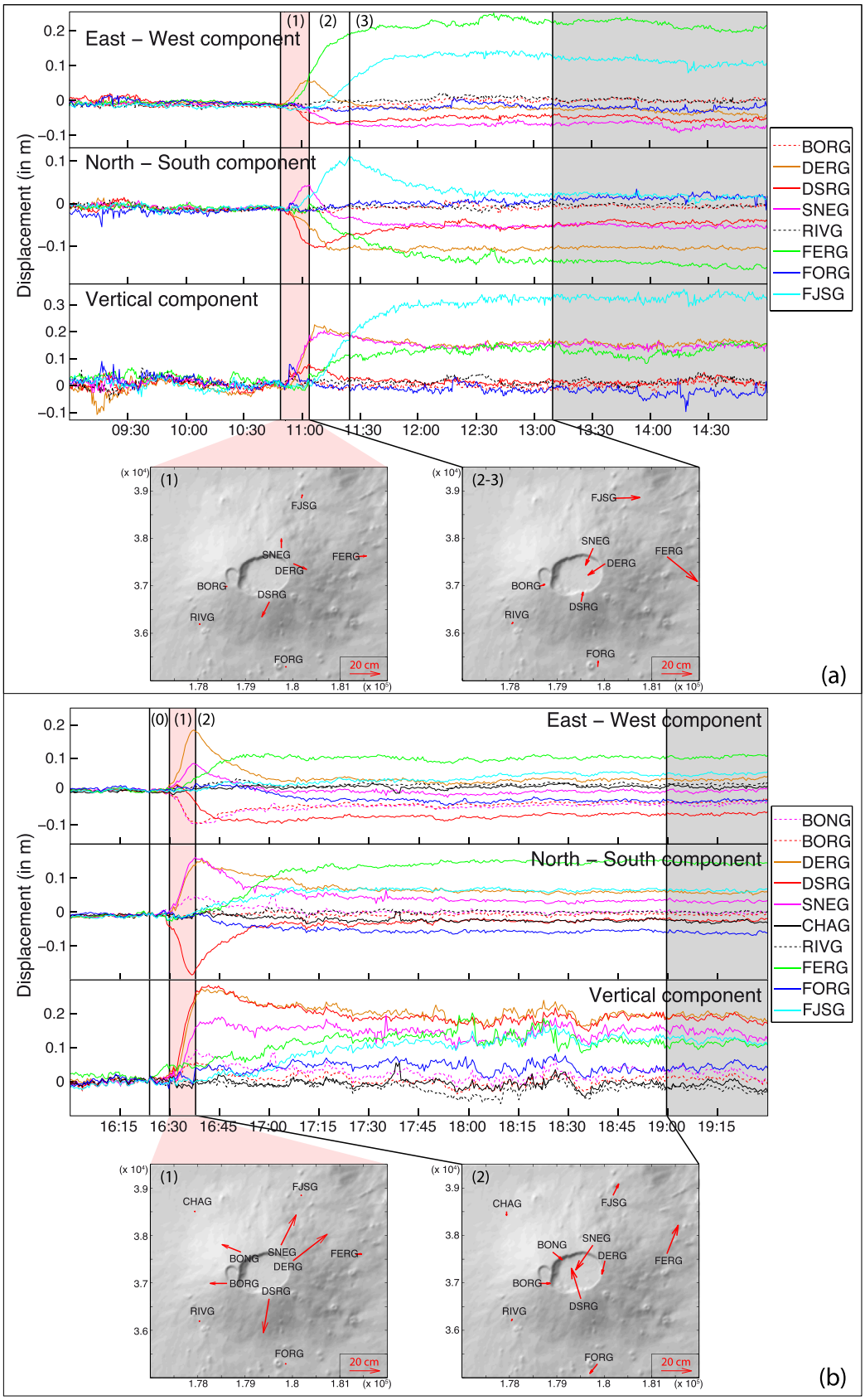

Figure 2. Ground displacements associated with distal dyke injections of (a) 26 December 2005 and (b) 30 March 2007 and recorded at the OVPF GPS stations. Labeled vertical solid lines correspond to the characteristic times presented in the results. Map sketches indicate the displacement vectors corresponding to each GPS station. Shaded grey areas indicate eruptive periods.

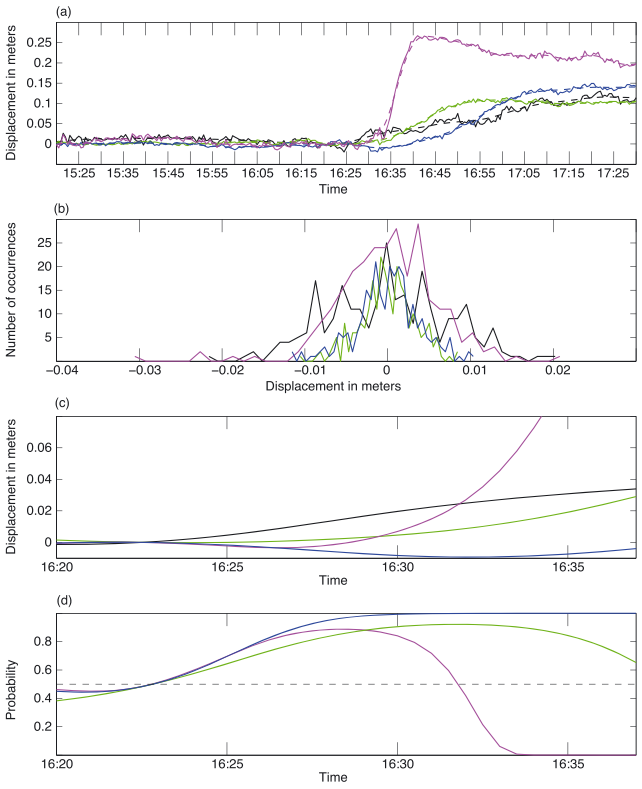

Figure 3. (a) Detailed representation of the ground displacement recorded by the FERG and DERG GPS stations. GPS displacement signals (solid lines); filtered GPS displacement signals (see text for cutoff frequencies; dashed lines); FERG vertical (black); FERG N-S (blue); FERG E-W (green); DERG vertical (magenta). Color codes are identical in all panels. (b) Estimation of the probability density function of the noise for the 15:20–16:20 displacement record. Noise is estimated as the residual of the signal after removing the filtered signal in the 1 h period preceding the displacements related to the magma transfer. (c) Detailed representation of the filtered displacements recorded by GPS stations at the initiation of the magma transfer. (d) Probability that the FERG vertical displacement was greater than displacements recorded on various GPS components, assuming a Gaussian distribution for the noise. See text for standard deviation estimations.

2.4. Low-Pass Filtering, Variance Estimation, and Probability Assessment

[11] Finally, we filtered the signal using a second-order Butterworth filter (Figure 3a). The filtered signal is an estimate of the mean value of the signal. Because signal and noise share a frequency interval, some low-amplitude, low-frequency noise components remained in the filtered signal. Mean values and standard deviations were both slightly biased by a few millimeters. The FERG low-pass-filtered vertical signal corresponded to a 25-sample average, so the standard deviation on that average was 5 times less than the standard deviation of each sample, that is, only 0.2 cm. The FERG horizontal and DERG vertical low-pass-filtered signals had similar standard deviations. These standard deviation estimates are lower bounds, as the sample standard deviation calculated from the filtered signals was underestimated by a few millimeters. An upper bound on the filtered signal standard deviation may be provided by the unfiltered sample standard deviation (1 cm). Using this latter estimate for each filtered signal, we first estimated the probability that the FERG vertical filtered signal would be larger than the FERG horizontal and DERG vertical filtered signals by computing the signal difference and its probability density function as a function of time. Because we consider the two signals to be independent, the variance of the signal difference is the sum of the two signal variances.

[12] The results of this analysis showed (Figures 3c and 3d) that at the onset of the FERG vertical signal between 16:25 and 16:30, the probability that the amplitude of that signal was larger than the amplitude of the FERG horizontal or DERG vertical signal was as high as 80%. The amplitudes of the horizontal components of FERG were close to the background noise between 16:25 and 16:30.

3. Results

3.1. Summit and Proximal Eruptions

[13] Displacements preceding these types of eruptions show that rapid summit inflation occurred (see the example of the 20 July 2006 eruption in Figure 5). No significant inflation was recorded by the basal stations (FERG, FORG, FJSG), and no summit deflation occurred before the beginning of the eruption.

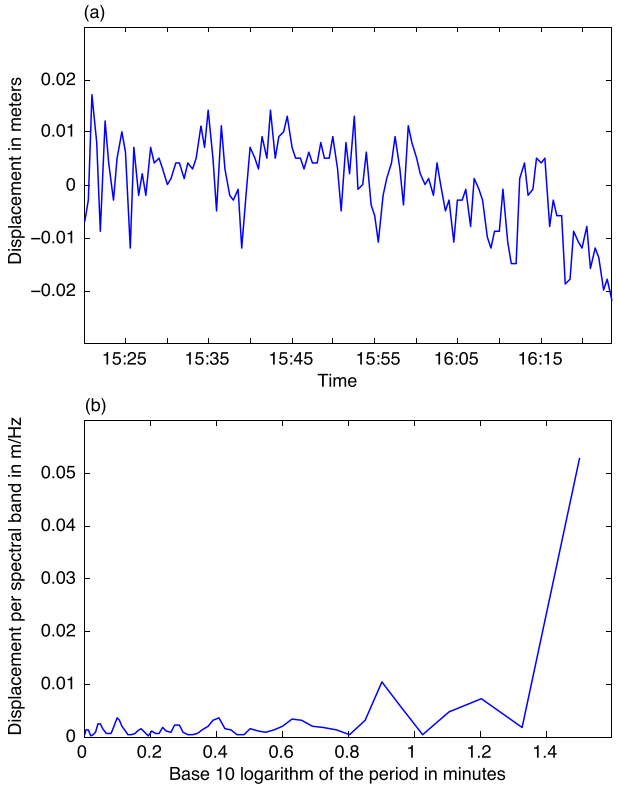

Figure 4. (a) One hour record of the FERG GPS vertical component noise measured before the 30 March 2007, strong displacement preceding the eruption. (b) Periodogram computed for the 1 h noise sample presented in Figure 4a.

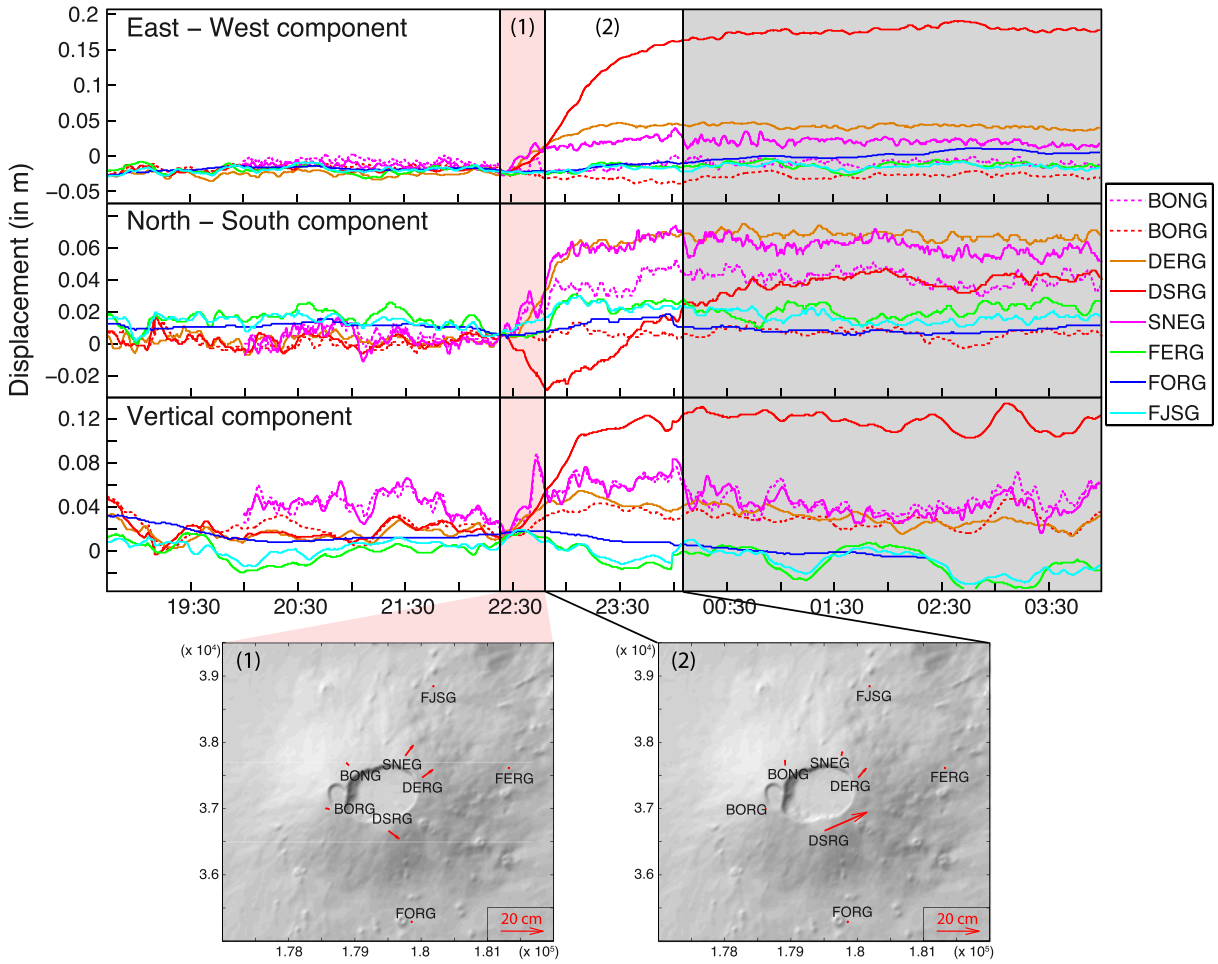

Figure 5. Ground displacements associated with the summit dyke injection of 20 July 2006 and recorded by the OVPF GPS stations. Labeled vertical solid lines correspond to the characteristic times presented in the results. Map sketches indicate the displacement vectors corresponding to each GPS station. Shaded grey areas indicate eruptive periods.

3.2. Distal Eruptions

3.2.1. The 26 December 2005 Eruption

[14] Figure 2a shows the ground displacements recorded during the magma injection that fed eruptive fissures located in the northern flank (Figure 1). The time history of the deformation process revealed three phases:

[15] 1. 10:50: Start of the rapid summit inflation recorded on the three components of DERG, SNEG, and DSRG, the eastward displacement of the eastern flank, measured at FERG, the northward displacement of FJSG; DERG eastward displacement occurred before its vertical displacement;

[16] 2. 11:05: Start of summit deflation; signal inversion of the E-W and vertical component of DERG, and N-S component of SNEG; start of the vertical inflation of the flanks measured at FERG and FJSG; sign of the concavity of the FERG E-W displacement changed, that is, eastward velocity measured at FERG was maximum; start of southward displacement at FERG, deflation at DSRG and downward displacement at DERG;

[17] 3. 11:25: Signal inversion of the N-S component of FJSG.

[18] FERG and FJSG recorded a large amount of final eastward and vertical displacement; eastward displacement is larger at FERG than at FJSG, whereas vertical displacement is larger at FJSG. Vertical displacement at the eruption time at FJSG is 3 times larger than horizontal displacement.

3.2.2. The 30 March 2007 Eruption

[19] Figure 2b shows the ground displacements recorded during this magma injection, which fed two eruptive fissures on the southern edge of the eastern flank (Figure 1). Again, this eruption took place in three distinct stages:

[20] 1. 16:25: Start of vertical displacement at the easternmost GPS station, FERG;

[21] 2. 16:30: Start of horizontal and upward displacements at the summit stations, and of eastward displacement at the easternmost station, FERG; start of rapid summit uplift;

[22] 3. 16:38: Start of the summit deflation; continuation of upward and N-E displacement at FERG and FJSG, and downward and S-W displacement at DSRG and DERG; maximum FERG eastward velocity (concavity inverted) was at maximum summit inflation (DERG, SNEG).

[23] Distal eruptions therefore share characteristic features (Figures 2a and 2b):

[24] 1. Simultaneous initiation of the eastward displacement of the eastern flank FERG station and of the rapid, three-component displacement of the summit stations; magma

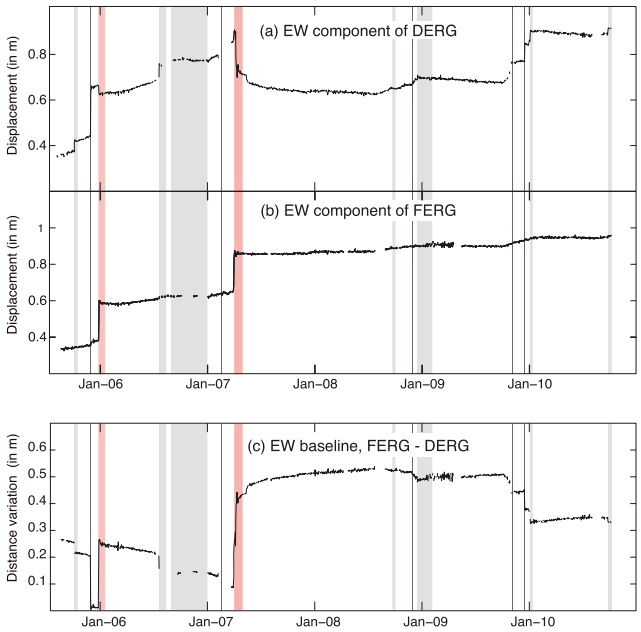

Figure 6. East-west daily averaged displacement recorded between 2005 and 2011 by the (a) DERG and (b) the FERG station; displacement is positive eastward; (c) E-W FERG-DERG baseline length; lengthening is positive. Shaded areas indicate eruptive periods (summit/proximal eruptions (grey); distal eruptions (red)).

propagates vertically below the summit; it is remarkable that in March 2007, the FERG station was displaced eastward then northward (with FORG and FJSG), the dyke finally propagating in a E-W direction in the south of FERG;

[25] 2. Simultaneous summit deflation and eastern flank inflation (eastward-upward displacement); magma propagates from the summit to the periphery;

[26] 3. Eruption follows summit deflation;

[27] 4. Large final eastward and upward deformation of the eastern flank (station FERG).

[28] Displacement records also showed differences between the two distal eruptions:

[29] 1. In 2005, the eastward displacement of the eastern flank FERG station was double to that recorded in 2007. In 2005, the dyke propagation direction was N35°; in 2007, it was N125° (Figure 1).

[30] 2. The thorough analysis of the 2 sample/min GPS signal recorded during 30 March 2007 eruption (see section 2) shows that magma transfer began with the upward displacement of the eastern flank FERG station (Figure 2b).

3.3. Long-Term Deformation Pattern

[31] Displacements and baseline changes computed from GPS position measurements show that DERG station (eastern Dolomieu) was displaced steadily eastward, DERG-BORG baseline lengthened (~5 cm), and FERG-DERG baseline shortened (~5 cm) during the inter-eruptive periods of 2005–2007 (Figures 6 and 7). During the 4 October and 29 November 2005 and 20 July 2006 proximal eruptions, large DERG eastward displacements occurred (5 to 20 cm), whereas FERG remained fixed, so that DERG-BORG strongly lengthened and FERG-DERG strongly shortened (Figures 6 and 7). Just before the onset of the 26 December and 30 March 2007 distal eruptions. DERG moved westward, FERG moved eastward (Figure 6), DERG-BORG strongly shortened (5 to 40 cm) and FERG-DERG strongly lengthened (20 to 30 cm).

[32] GPS rapid-static reiterated measurements were first used to investigate horizontal displacements between distal

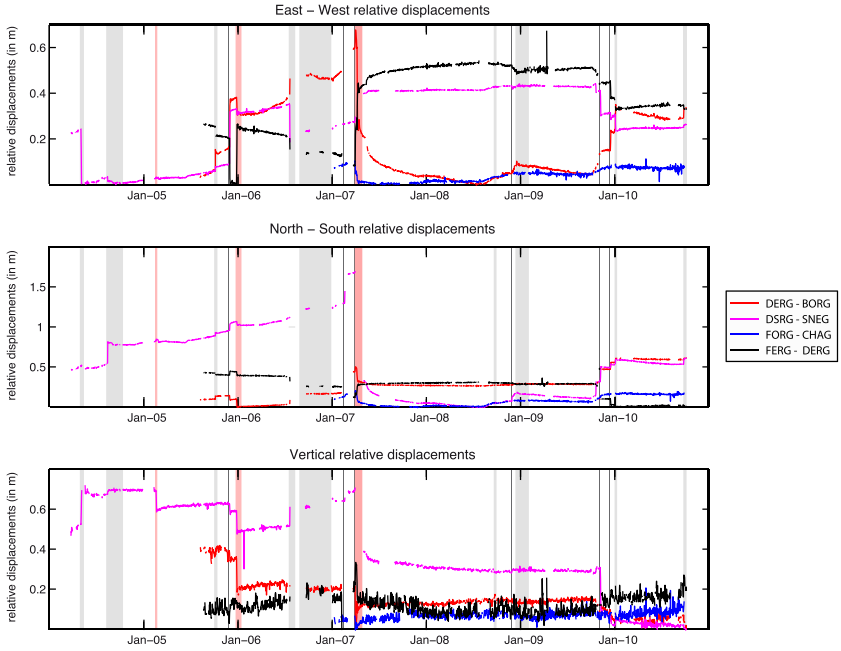

Figure 7. Baseline changes recorded for four station pairs between 2004 and 2010. Shaded areas indicate eruptive periods (summit/proximal eruptions (grey); distal eruptions (red); see Table 1 for details). Distance samples are daily averages.

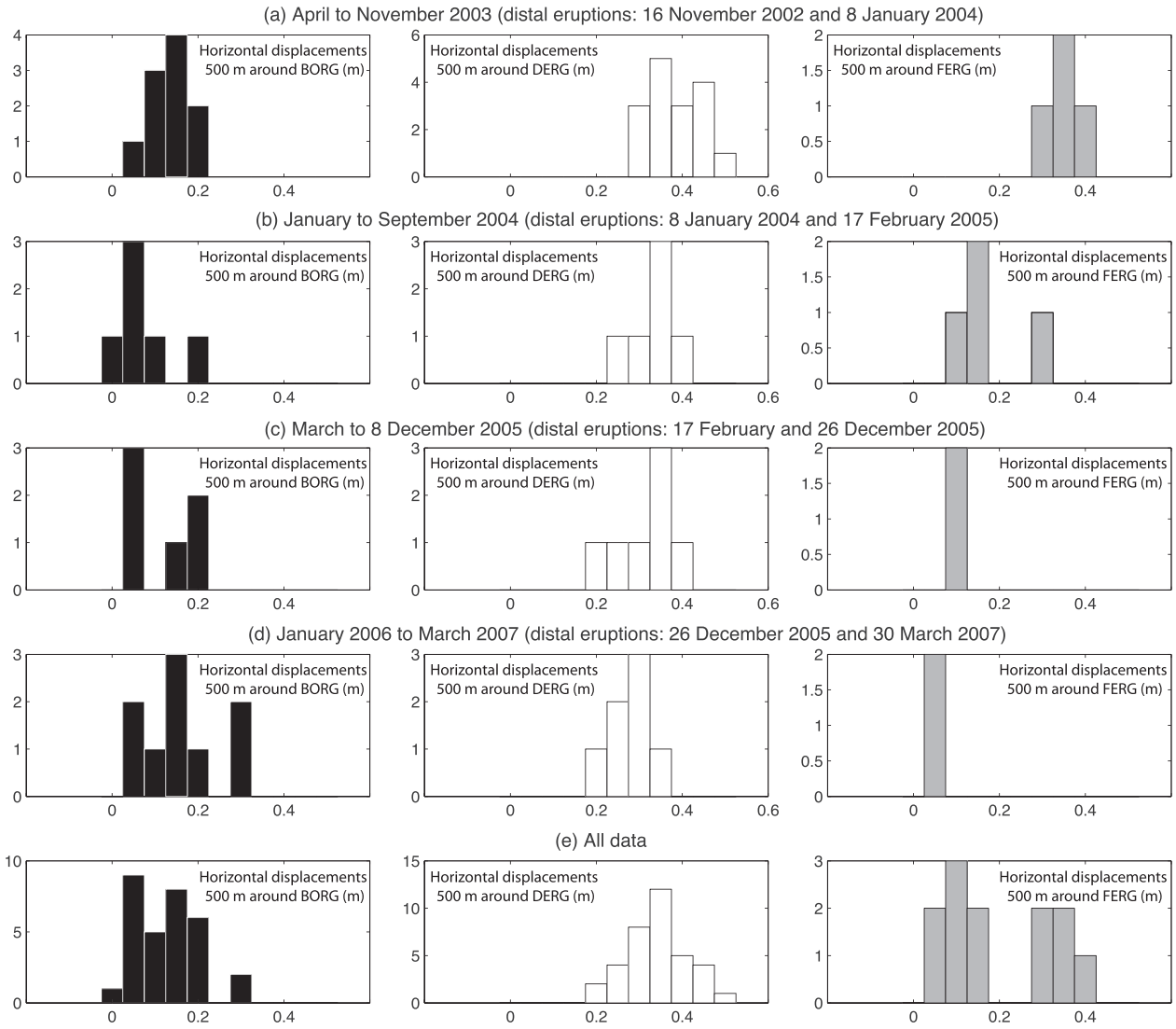

Figure 8. Histograms of the horizontal displacements recorded at benchmarks located within a 500 m distance around BORG, DERG, and FERG GPS stations; (a–d) for each of the four interdistal periods occurring during the time where the reiterated GPS network was installed; (e) gathering all interdistal displacements of these four periods. Notice the weak displacement of the FERG GPS station during the interdistal period preceding the major distal eruption of March–April 2007. Larger displacements around FERG (Figures 8a and 8b) were recorded during the intrusion of 6 November 2003 and the proximal eruption of 12 August 2004, where eruptive fissures opened close to FERG.

eruptions (Figure 8). Around DERG, their sample distribution exhibited a clear mode corresponding to a more frequent horizontal displacement and a mean close to 35 cm (Figure 8e), with amplitudes ranging from 20 to 50 cm. Around BORG, the sample distribution showed no clear mode, amplitudes ranging from 0 to 30 cm, with an average close to 10 cm. Interdistal horizontal displacements are therefore more than 3 times larger at DERG than at BORG, most of the differential displacement occurring during summit/proximal eruptions. The sample distribution of these displacements is remarkably structured at DERG, showing a clear mode; it evokes a characteristic displacement plus a limited random noise, whereas no such feature emerges from the sample distribution of the displacements measured around BORG. Another important and characteristic feature is the fact that FERG exhibited generally a few displacements during the same period, except in the case a proximal eruption occurred near this station. As an example, during the interdistal period preceding the March–April major distal eruption, FERG exhibited less than 5 cm horizontal displacement, whereas DERG (located 1.4 km westward) exhibited 30 cm horizontal displacement.

[33] Average displacement of each benchmark was computed using these measurements (Figure 9) for 11 summit/proximal and four distal eruptions. They show that during summit eruptions, there are systematic summit inflation and no upper eastern flank displacement. During distal eruptions, there is a systematic large eastward and upward displacement of all benchmarks located in the upper eastern flank, whereas there are very few displacements in the western flank. Remarkably, whatever can be the location and direction of the dykes

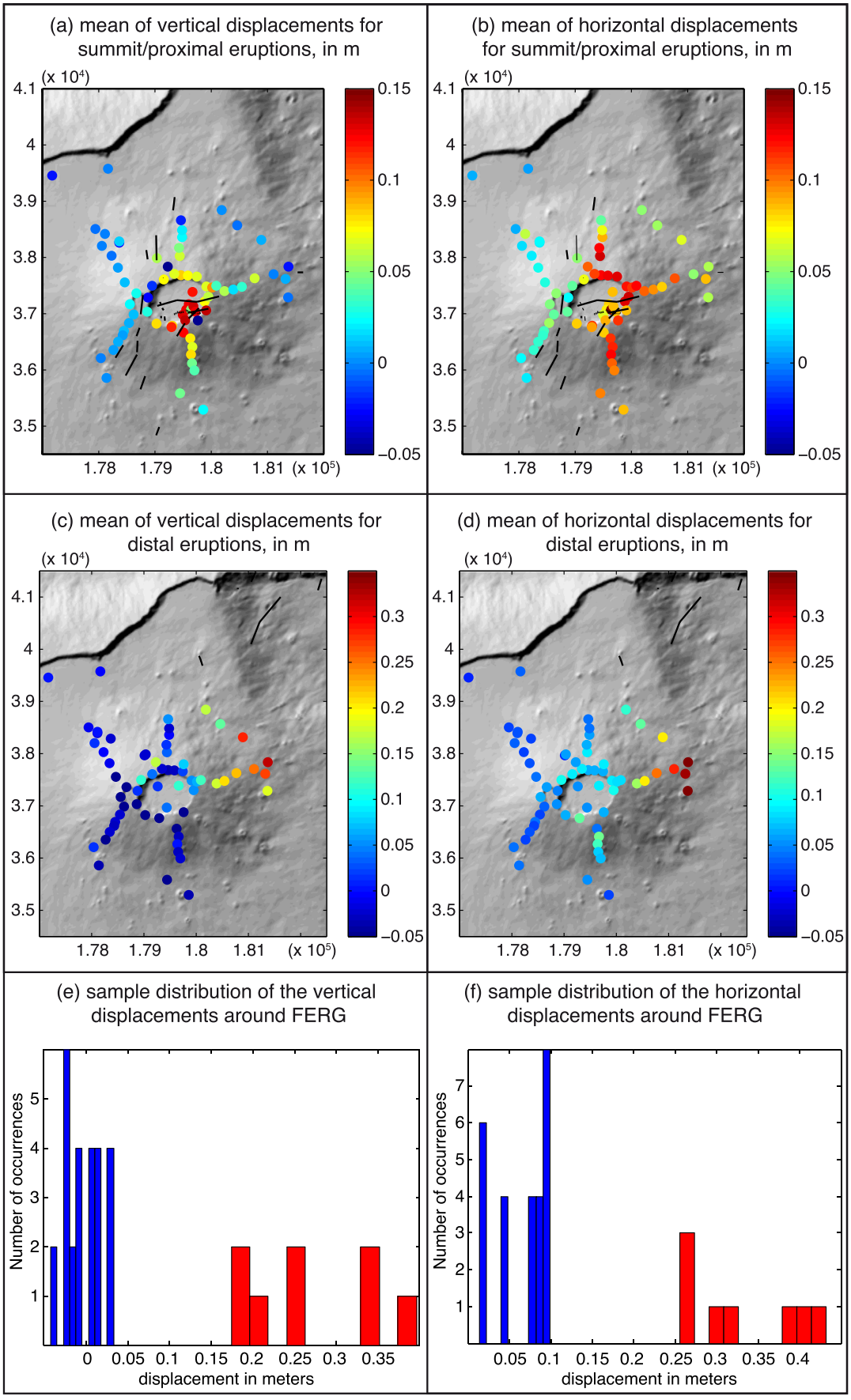
(a) mean of vertical displacements for summit/proximal eruptions, in m
(b) mean of horizontal displacements for summit/proximal eruptions, in m
(c) mean of vertical displacements for distal eruptions, in m
(d) mean of horizontal displacements for distal eruptions, in m
(e) sample distribution of the vertical displacements around FERG
(f) sample distribution of the horizontal displacements around FERG
(x 10⁴)
(x 10⁵)
Number of occurrences
displacement in meters

Figure 9

involved in the distal eruptions [e.g., *Peltier et al*., 2008, 2009a], displacements in the upper eastern flank around FERG are systematically 3 to 5 times larger during distal eruptions than during summit/proximal eruptions (Figures 9e and 9f).

4. Understanding Edifice's Deformation and State of Stress

4.1. The Importance of Rock Rheology in Understanding the Volcano's Deformation

[34] When trying to understand volcano's deformation, data are often surface displacements and the parameters are rock rheology and the geometry of the pressure source. Considering this problem with a Bayesian probabilistic point of view, we could assign some probability to both data and parameters. Data probability density functions can be inferred directly from measurements (e.g., surface displacements). Parameters are not directly measured but we have some a priori knowledge on them. Most studies involved in deformation modeling using an inversion process assign an implicit very strong probability to the rock rheology and consider it as elastic; they do not take into account any a priori knowledge on the geometry of the source pressure and infer this geometry from the displacements measured at the surface only, given an implicitly perfectly known elastic rheology. In this work, we will take the opposite point of view: We will consider that the a priori knowledge about the geometry has more probability than the knowledge of the rheology. We will therefore investigate how rheology may be constrained by surface displacements, knowing pressure source geometry. A priori information on rock rheology will arise from a preliminary analysis of the data (surface displacements), which will lead to the choice of a rheological law. In our study, a priori information probability on geometry will come from dyke dip measurement statistics and previous geophysical studies at Piton de la Fournaise. In this first approach, although we will explore the problem quite thoroughly, we will not attempt a complete inversion. Our aim is to show that nonelastic rheology may provide pertinent models, which are compatible with both geological information and surface displacements at different time periods of the eruptive cycle evidenced at Piton de la Fournaise volcano. We will first consider the first-order, long-wavelength characteristics of the surface displacements, then their second-order variations. These models will be used to design a synthetic view of the volcano's long-term dynamics.

4.1.1. Relation Between Asymmetry of the Deformation of the Piton de la Fournaise Volcano and Edifice Rheology

[35] Continuous and rapid-static GPS measurements show a strong asymmetry in the edifice's deformation, which appears to be a major characteristic of the volcano: The eastern flank deforms many times more than the western flank, especially during distal eruptions. Geologic observations allow to evidence the sample distribution of dyke dips [*Letourneur et al*., 2008; *Peltier et al*., 2012]. They show that this distribution is unimodal, the mode corresponding to a subvertical dip. Elastic modeling of surface deformation performed with subvertical dykes does not allow to explain the E-W displacement asymmetry. Modeling such an asymmetry using an elastic rheology implies nonvertical dykes [*Fukushima et al*., 2005; *Peltier et al*., 2007]. *Letourneur et al*. [2008] used a bimaterial edifice, with a Young modulus lower (5 MPa) in the eastern flank than in the western flank, and a concave dyke, in such a manner, the concavity concentrated the deformation in the eastern flank. However, dyke opening is a mode of deformation of the edifice, and the concavity of the dyke arises from the stress field which creates it; moreover, using a bimaterial implies choosing the boundary between the materials, which strongly constrains the asymmetry of the computed surface displacements.

[36] The problem of the asymmetry in the edifice surface deformation refers to the edifice fundamental state of stress and cannot be understood without taking into account the surface topography, gravity, and rock rheology. Strain measured from 2003 to 2007 along the BORG-FERG and DERG-FERG baselines was strong ($\sim 10^{-3}$), with the upper eastern flank (FERG) moving eastward whereas the western flank was stable. Such a deformation regime lasts for years, so that deformation exceeds the rock elastic limit, especially in tension. Geological observations in the caldera walls (Remparts and Dolomieu) show that rock is deeply fractured [*Bachèlery*, 1981; *Michon et al*., 2009; *Peltier et al*., 2012].

[37] Distal eruptions are systematically (whatever can be the orientation of the dyke) associated to a large displacement (~30 cm) of the upper eastern flank (FERG) whereas it is only less than 10 cm for summit/proximal eruptions (Figure 9): Eastward/upward displacement at FERG is therefore quantized, a pattern which is interpreted as the result of a threshold effect in physics. Interdistal horizontal displacement distribution at DERG (Figure 8e) shows a clear mode corresponding to a characteristic amplitude, and therefore to a characteristic horizontal stress intensity. All these observations show that the elastic limit is reached in the eastern flank during distal eruptions and that the large displacements that occur during distal eruptions are in part anelastic and irreversible, and may be characterized as due to an elastoplastic deformation, rather than to a purely elastic one.

4.1.2. Modeling the Asymmetry of the Surface Displacements at Piton de la Fournaise Volcano

[38] To check this elastoplastic conjecture for the edifice rheology and understand better the eastern flank deformation during distal eruptions, we model the Piton de la Fournaise volcanic edifice by using a 2-D plane strain elastoplastic rheology, taking into account the topography and gravity. We model the plasticity threshold by using a Drücker-Prager criterion [*Drücker and Prager*, 1952], which increases with the isotropic tensor without having the yield surface singularities of the Mohr-Coulomb criterion in the principal stress space: Drücker-Prager criterion is continuously differentiable with respect to stress. As it may be considered as a smooth version

Figure 9. Map of the average (vertical and horizontal distances) ground displacements during (a, b) summit/proximal and (c, d) distal eruptions, measured on the reiterated OVPF GPS network. Solid lines represent the associated eruptive fissures. (e, f) Sample distribution of the vertical and horizontal displacements (summit/proximal eruptions (blue); distal eruptions (red)) recorded in the upper eastern flank, around the FERG GPS permanent station.

of the Mohr-Coulomb criterion, it may be expressed in terms of the internal friction angle ϕ and the cohesion C:

$$\sqrt{J_2} = \alpha I_1 + K,$$

where J_2 is the second invariant of the deviatoric stress tensor (that is, $\sqrt{J_2}$ is the quadratic norm of this tensor), I_1 is the first invariant of the stress tensor (that is, 3 times the lithostatic pressure), and, in plane strain formulation, using the associated form of the criterion

$$\alpha = \frac{\tan\phi}{\sqrt{9 + 12\tan^2\phi}} \quad \text{and} \quad K = \frac{3C}{\sqrt{9 + 12\tan^2\phi}}.$$

[39] In our model, when the quadratic norm of the deviatoric tensor reaches this plasticity threshold, the rock has a perfectly plastic rheology. The volcanic edifice is constituted by a homogeneous elastoplastic material: The spatial distribution of the deformation is therefore constrained by the spatial distribution of the points where the deviator reaches the plastic threshold, not by an imposed and specific spatial distribution of the rheology. The Drücker-Prager (and Mohr-Coulomb) plasticity threshold (that is, the rock yield strength) increases with I_1 (that is, with the mean stress and therefore with depth). At a given altitude in the edifice, the depth from the free surface below the eastern flank is lower than the depth from the free surface below the western flank, so that the plasticity threshold is lower below the eastern flank than below the western flank. In these conditions, any pressure source placed below the summit will induce more deformation in the eastern flank than in the western flank.

[40] In our 2-D model, we will consider as a priori known, from geological observations, the dip of the dykes, and we will assume them to be vertical and normal to the E-W cross-section plane. From former results of *Peltier et al*. [2008, 2009a], we know that dykes originate from below the eastern (western) part of the Dolomieu crater for distal (summit/proximal) eruptions. We impose a moderate overpressure (5 MPa) at the dyke boundaries. Young modulus of the edifice is 50 GPa; this is the Young modulus of the intact rock, anelasticity being taken into account by the plastic deformation. Dyke stiffness is 5 GPa (considering that the rock volume containing the dyke is made from the edifice rock, damaged at 90%, following the linear damage approach of *Kachanov* [1958; see also *Valko and Ekonomides*, 2001]); this value does not limit the displacement of the dyke boundaries. A trade-off exists between the dyke pressure, apparent width, and Young modulus: Similar displacements may be reached at the dyke boundaries using various combinations of these parameters. Finite element implementation of this model and the following were practically performed by using the COMSOL high-level modeling package.

[41] We first compare the displacements computed with homogeneous elastic and elastoplastic models with the displacements measured for distal eruptions (Figure 10) along an E-W profile. The displacements measured along this profile are strongly asymmetric. Elastic models with vertical dykes (Figure 10) were not able to account for this asymmetry. This asymmetry is retrieved for an internal friction angle ϕ of 15° and a cohesion C of 1 MPa. These values correspond with those found in deep drilling cores of the Kilauea Volcano [*Schiffman et al*., 2006]. These results therefore show that an elastoplastic rheology with realistic elastic and plastic parameters for the whole edifice accounts for the observed asymmetry of the surface displacements during a distal eruption, even in the case where dykes are vertical, as inferred from geological field observations and statistics. Observations and modeling show that the displacement asymmetry and therefore most of the upper eastern flank displacement are due to plastic deformation, and give some bounds to the elastic/plastic partition of the deformation in this flank. *Norini and Acocella* [2011] recently reached comparable results by using analog experiments in granular media.

4.1.3. Modeling Second-Order Surface Displacements Variations: Evidences of Strain Weakening in the Edifice

[42] Interdistal surface displacement is mostly far larger at DERG than at FERG; it was especially the case from 2005 to 2007 where DERG experienced a 20 cm eastward displacement whereas FERG experienced only a 3 cm eastward displacement. Asymmetry between western and eastern Dolomieu rims (BORG and DERG) and strong displacement gradient in the upper eastern flank (DERG and FERG) are difficult to explain with a simple $\phi = 15°$ elastoplastic model, as increasing ϕ decreases the BORG-DERG asymmetry, and decreasing ϕ increases the displacement at FERG. Displacement at DERG is anomalously high whereas at FERG it is anomalously low. This feature leads us to investigate the influence of the pressure sources and of ϕ in the edifice, as well as other model parameters, on the surface displacements. We therefore model the edifice as an elastoplastic edifice ($E = 10$ to 80 GPa, $\phi_{\text{Edifice}} = 15$ to 40°) containing an oblate reservoir submitted to an internal pressure (varying between −20 and 20 MPa) applied to its boundary. The reservoir was located at a depth varying from 0 to 1600 m below the Dolomieu crater. Its radius varied from 200 to 1600 m. The edifice is loaded by a vertical dyke source pressure located at the western end of the Dolomieu crater, as most of the interdistal displacement arises during summit/proximal eruptions. Dyke height and overpressure varied respectively from 200 to 1000 m and from 5 to 40 MPa. A sensitivity study of the surface displacement with each of these parameters shows (Figure 11) that displacement at the basis of the summit cone (e.g., at FERG) is lower when the dyke height, the reservoir overpressure, and ϕ_{Edifice} are low, and when the edifice Young modulus, the reservoir radius, and elevation are high. Intervals for the variation of these parameters are inferred from previous studies [e.g., *Peltier et al*., 2007, 2008, 2009a, 2009b]. Therefore a model in which reservoir radius is 1 km, altitude is 1000 m, underpressure is 20 MPa, and dyke height is 300 m (parameters close to extreme bounds issued from the previous studies) allows fitting the data using the lowest possible values of ϕ_{Edifice} (Figure 12). Theoretical displacements show that the minimum values for ϕ_{Edifice} to fit the data, especially near FERG, are larger than 30°. Whatever can be the values of the parameters other than ϕ_{Edifice}, models fitting correctly interdistal displacements have high ϕ_{Edifice}; especially, models with low ϕ_{Edifice} never account for low displacement values at FERG.

[43] Such computations show that during interdistal periods ϕ_{Edifice} remained significantly larger than during distal

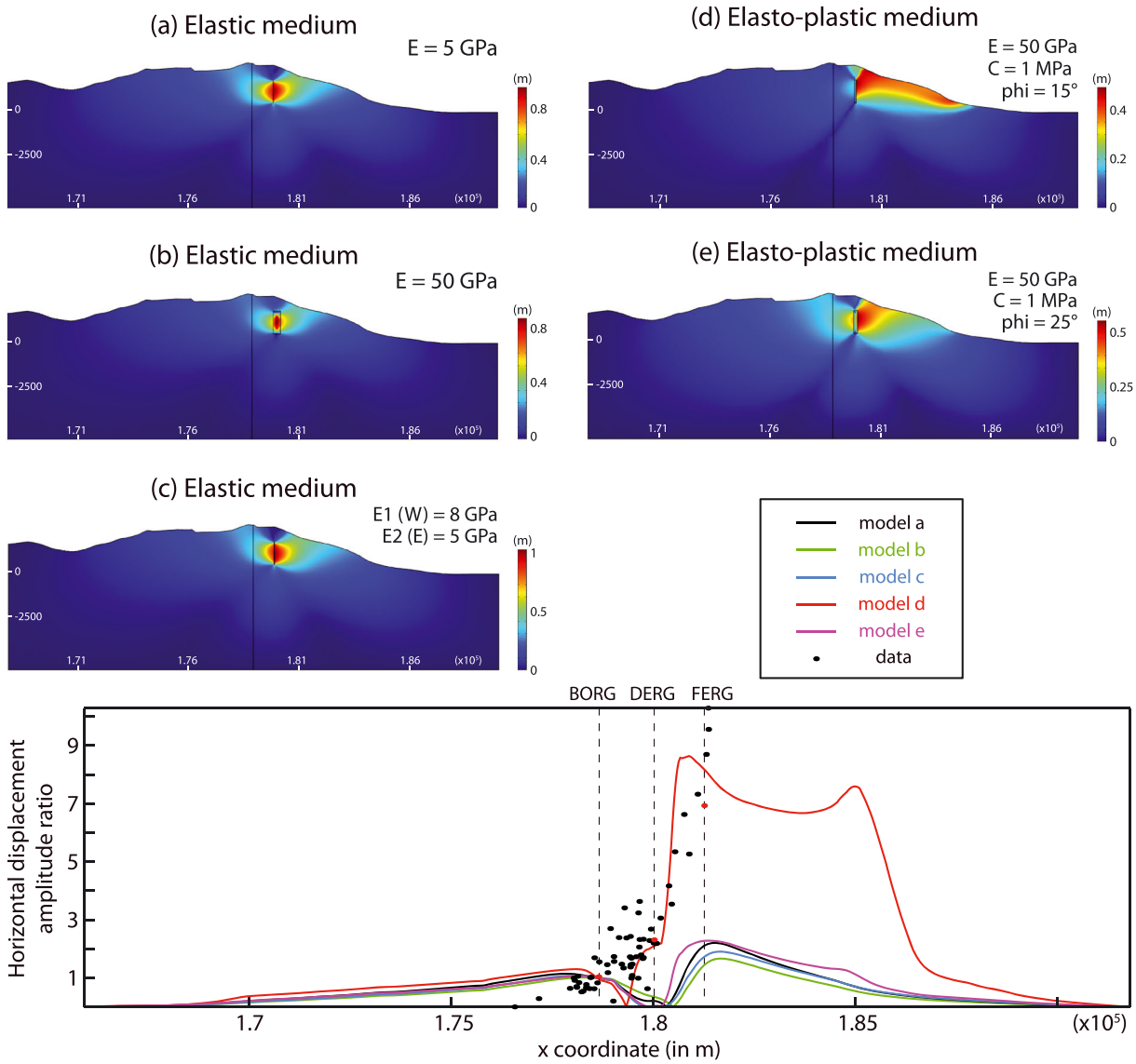

Figure 10. Results of the 2-D (E-W cross section) numerical modeling of the displacements recorded during distal eruptions, using a vertical pressurized dyke located in the eastern part of the Dolomieu crater and various rheologies for the volcanic edifice, characterized by their Young modulus (E), cohesion (C), and internal friction angle (ϕ). Elastic rheology (a) $E = 5$ GPa and (b) $E = 50$ GPa; (c) bielastic rheology, with an 8 GPa Young modulus in the western part of the edifice and a 5 GPa Young modulus in the eastern part, following *Letourneur et al.* [2008]; the limit between the eastern and western part of the edifice is represented by the vertical line issued from the summit, at the western end of the Dolomieu crater, following *Letourneur et al.* [2008]; (d) elastoplastic rheology $E = 50$ GPa, $C = 1$ MPa, $\phi = 15°$, and (e) $E = 50$ GPa, $C = 1$ MPa, $\phi = 25°$. (f) Horizontal displacement amplitude ratio as a function of the longitude in meters. The ratio is computed from the horizontal displacement recorded at each measurement point, normalized by its value at the BORG GPS station. Amplitude ratios computed from the average of the horizontal component of the displacements measured for each distal eruption (January 2004, February 2005 and December 2005) occurring between 2002 and 2005, along the E-W profile containing the BORG, DERG and FERG GPS stations (black dots; see Figure 1). Amplitude ratios computed from the horizontal components of the displacements measured for the 30 March 2007 distal eruption, at the BORG, DERG and FERG GPS permanent stations (red dots). Amplitude ratios computed from the surface theoretical displacements computed for the various models (solid lines). The asymmetry in the displacements along an E-W profile is accounted by the low ϕ elastoplastic model only.

eruptions. Most of the displacement occurred at low yield strength during distal eruptions, whereas stress was accumulated up to a higher threshold during interdistal eruptions: This pattern reveals that strain weakening is likely to occur when the edifice ruptures during distal eruptions. The following paragraph will give a possible physical mechanism explaining how such a strain weakening may suddenly occur during distal eruptions.

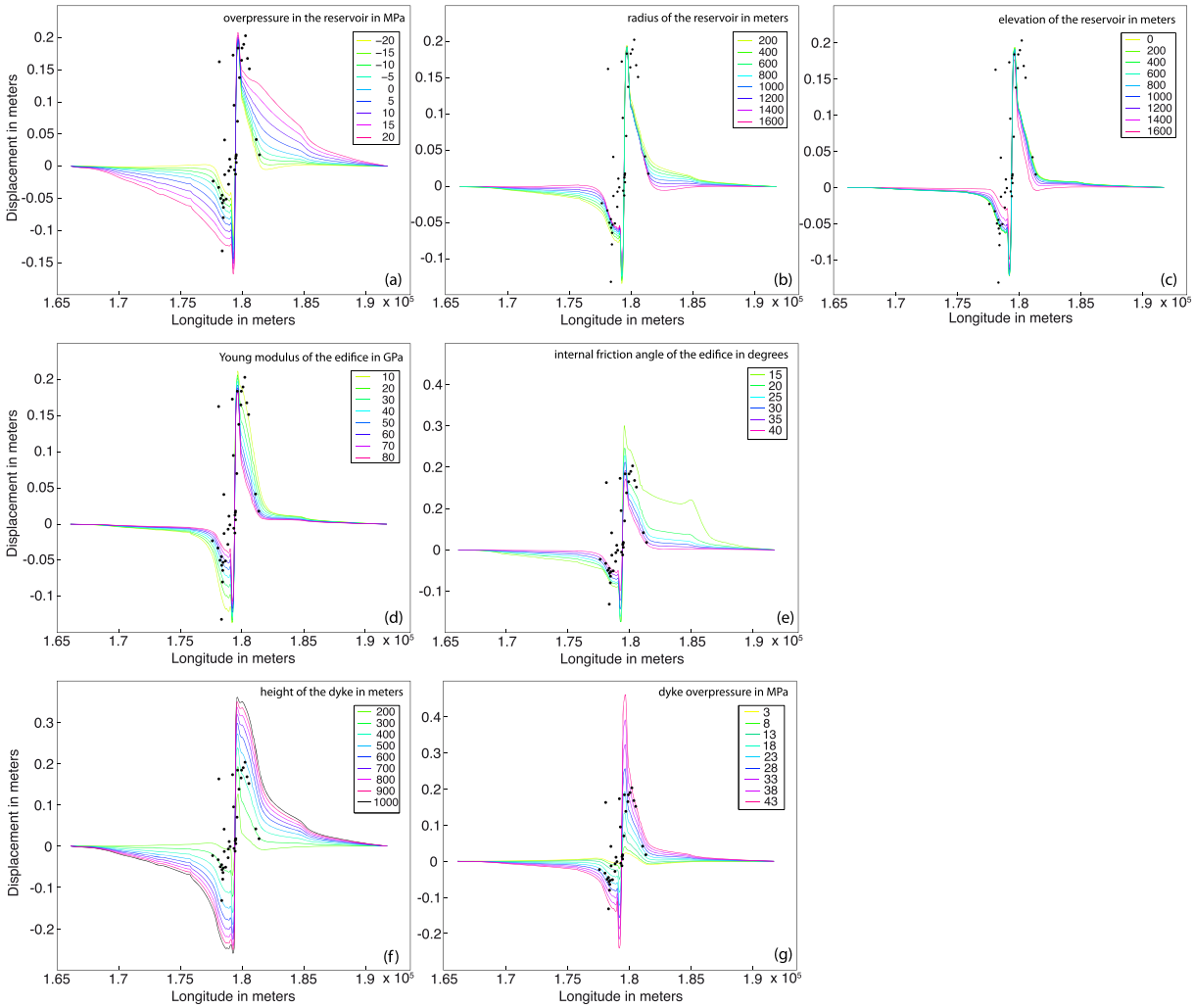

Figure 11. Results of the parametric study of the theoretical displacements as a function of longitude, for various model parameters: (a) reservoir overpressure ΔP_r, (b) reservoir radius R, (c) reservoir elevation Z_r, (d) edifice Young modulus E, (e) ϕ_{Edifice}, (f) dyke height H, (g) dyke overpressure ΔP_d. In each case, parameters that do not vary take the following values: $\Delta P_r = 0$ MPa, $R = 1000$ m, $Z_r = 500$ m, $E = 50$ GPa, $\phi_{\text{Edifice}} = 30°$, $H = 500$ m, $\Delta P_d = 15$ MPa. Black dots represent 2005–2007 interdistal mean horizontal displacements for benchmarks of the reiterated GPS network located at less than 500m distance of the E-W profile (Figure 1, see text for more details); the corresponding displacement distribution is represented in Figure 8d.

4.1.4. Detailed Insight Into Distal Eruptions

[44] During 30 March 2007 eruption, magma transfer began with the upward displacement of the eastern flank FERG station (Figure 2b). The vertical to horizontal stress ratio corresponding to a given vertical upward deformation along a horizontal plane accompanied by a null horizontal deformation along a vertical plane in an elastic medium is

$$\frac{\sigma_{zz}}{\sigma_{xx}} = \frac{1-\upsilon}{\upsilon}. \tag{1}$$

[45] Using a Poisson coefficient υ of 0.25, equation 1 gives $\sigma_{zz} = 3\sigma_{xx}$. Such stress and deformation states occur for example when a horizontal or subhorizontal (dip lower than 10°) planar structure embedded in an elastic medium is loaded with an internal pressure. Alternative explanations may be examined. For example, shear stresses acting on vertical planes causing vertical deformation at FERG and no deformation at DERG between 16:25 and 16:30 may have involved a source close to FERG moving vertically. Shear stresses are generally accompanied by normal stresses, which would cause horizontal deformation. This did not occur at this time. The displacement pattern recorded at FERG at the onset of magma transfer is therefore more likely to have been due to a subhorizontal pressurized structure. Such structures (sills) showing evidence of shearing have been reported in the Piton des Neiges volcano, La Réunion Island [*Famin and Michon*, 2010]. Pressurization and shearing of these structures may initiate flank displacements and distal eruptions. They provide a physical mechanism for the sudden occurrence of strain weakening during the eruptive cycle by the localization of the plastic deformation along a weak layer—a rupture-type process finally close to a slow earthquake or slow slip event, as those observed in the southern flank of Kilauea [*Cervelli et al.*, 2002; *Segall et al.*, 2006; *Brooks et al.*, 2006]. The internal friction angle does not change in a large volume of the

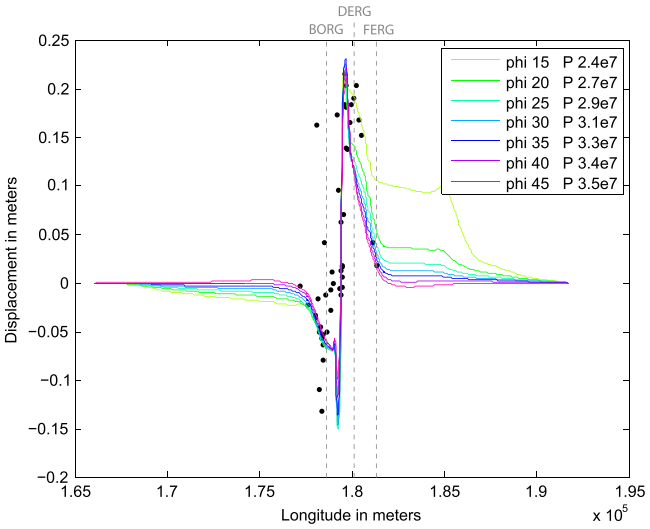

Figure 12. Interdistal mean horizontal displacements (same as Figure 11) and theoretical displacements computed for various values of ϕ, for the model described in section 4.1.3. In each case, dyke overpressure is adapted to get the observed displacements at the dyke boundaries, whereas ϕ controls the displacement at the base of the summit cone (westernmost and easternmost values). Low ϕ values do not allow to fit the observed displacement at FERG.

edifice—rather, its change may be understood as an observation of the bifurcation from diffuse to localized (fluid and solid) deformation.

4.2. Understanding Eruptive Cycles as Stress Cycles Before the Major Eruption of March–May 2007

[46] Two-dimensional elastoplastic models deduced from the fit of the surface displacement ratios allow to understand the series of deformation and stress changes occurring during an eruptive cycle (Figures 13 and 14). The edifice underwent stronger inflation at summit stations than at flank stations during inter-eruptive periods: DERG-BORG baseline lengthened whereas DERG-FERG baseline shortened (Figures 6 and 7). The progressive inflow and pressurization of the magma induce horizontal tension above the reservoir and horizontal compression in the flanks (Figure 14). No deflation occurred after eruptions, and inflation often started rapidly, at a remarkable steady rate, after eruptions. This reveals continuous magma input in the reservoir. Inflation was limited to less than ~10 cm (Figure 6), that is, ~100 microstrain, which may suggest an elastic process; however, the occurrence and acceleration in seismicity 2–4 weeks before eruptions [*Collombet et al*., 2003; *Schmid et al*., 2012] show that anelastic deformation and damage also occurred during this stage, especially at its end.

[47] When horizontal tension reaches the rock tensile strength in a sufficient volume, deformation accelerates, rock ruptures, and magma rises up (Figures 2 and 5) in a dyke. During summit/proximal eruptions, the BORG-DERG summit baseline length increases, and the DERG-FERG baseline length decreases (Figure 7); no upper eastern flank displacement is observed (FERG station, Figure 6). These deformation features are well reproduced by models (Figure 12), which show that summit/proximal eruptions load the summit edifice, where horizontal stress increases (Figure 14). Summit/proximal eruptions provide most of the summit interdistal displacement recorded at DERG (Figure 7); summit interdistal horizontal displacements exhibit a characteristic amplitude and therefore correspond to a characteristic horizontal stress intensity. As stress accumulated in the summit edifice repeatedly shows a maximum value and does not reach infinity as should be expected in a purely elastic edifice submitted to repeated pressurized magma injections, it is extremely likely that this characteristic stress corresponds to the yield stress of the volcanic edifice. As shown in section 4.1.3, this yield stress corresponds to a high ϕ value (an internal friction angle greater than 30°) during interdistal periods.

[48] At the initiation of the ~2 h pre-eruptive displacements recorded before a distal eruption, horizontal displacement preceded vertical displacement at DERG (2005), DSRG, DERG, and SNEG stations (2007) (step 1, Figure 2); eastward displacement of FERG preceded its northward displacement. This eastward displacement loads the eastern flank and triggers the large eastward displacement of upper eastern flank FERG station. This latter displacement is clearly far larger than that recorded at BORG during the same eruption, and at FERG during summit/proximal eruptions and interdistal periods (Figures 2, 8, and 9). Modeling of the displacements (large in the eastern flank) recorded during distal eruptions (Figure 10) shows that ϕ is as low as 15°; that is, yield stress is lower during distal eruptions than during interdistal periods: Strain weakening occurs. During step 1 (Figure 2), plastic displacement occurs in the eastern flank; it relaxes the horizontal stress (Figure 14c), increases the edifice volume, and induces the reservoir pressure drop. Summit deflation occurs (Figures 2 (step 2) and 14d). At the onset of summit deflation, summit acceleration is directed downward; that is, gravitational and elastic reaction forces of the edifice are larger than the pressure forces applied by the fluid (magma) on the edifice: The edifice loads the fluid. FERG eastward displacement rate remained constant at the onset of summit deflation (Figure 2): This shows that summit deflation perfectly balanced the stress/pressure drop induced by the initial eastern flank displacement. It restitutes elastic and gravitational potential energy accumulated during the interdistal periods and provides energy for continuing eastern flank and magma displacement (Figure 13d): Deep material, especially magma, is displaced from the reservoir to the eastern flank and provokes the eastward-upward inflation of the eastern flank. This process provides an explanation to the location of the distal eruption itself. Modeled elastoplastic displacements may also explain, with a simple source geometry (and a simple nonlinear rheology), the large displacements found in the eastern flank by interferometric synthetic aperture radar interferometry [*Tinard*, 2007; *Augier et al*., 2008; *Clarke et al*., 2013], which would need a complex source geometry to be explained using a linear elastic rheology [*Augier*, 2011]. At the end of a distal eruption, the deep eastern flank is loaded whereas the summit edifice is in horizontal tension (Figure 14). Notice that during magma transfer process leading to a distal eruption, the summit stress field changes very rapidly, from a compressive horizontal stress at the beginning of the process (step 1) to a tensile one at the end of the process (steps 2 and 3; Figures 2 and 14).

[49] The eruptive cycle evidenced by *Peltier et al*. [2008] therefore corresponds to a stress cycle, where the plastic displacement of the eastern flank during distal eruptions allows to periodically relax the elastic stress accumulated during the

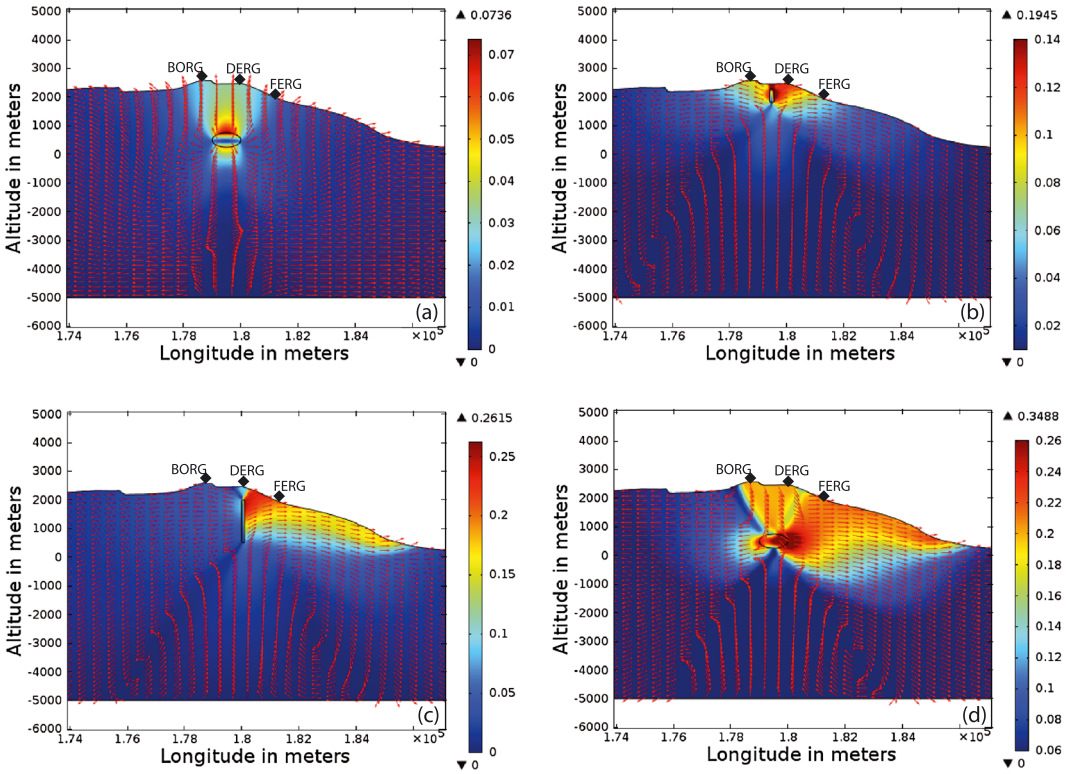

Figure 13. Theoretical displacement amplitude (color, in meters) and direction (arrows) as a function of the longitude and altitude, for various loading cases, during the eruptive cycle: (a) inter-eruptive periods: The elastoplastic edifice ($\phi = 30°$, $C = 1$ MPa) is loaded by an elliptical pressurized (overpressure: 5 MPa, altitude: 500 m, radius: 500 m, height: 250 m) reservoir located below the Dolomieu crater; deformation is limited to the summit cone; (b) summit/proximal eruptions: The elastoplastic edifice ($\phi = 30°$, $C = 1$ MPa) is loaded by a pressurized vertical dyke (overpressure: 10 MPa), deformation is weak outside the summit cone (see Figures 6–9 for observed displacements); (c) step 1 (Figure 2) of the distal eruption displacements, early large eastward displacement of the eastern flank and eventual localization of the deformation along a sill structure: The elastoplastic edifice ($\phi = 15°$, $C = 1$ MPa) is loaded by a pressurized vertical dyke (overpressure: 5 MPa) located in the eastern part of the Dolomieu crater; (d) step 2 (Figure 2) of the distal eruption displacements: summit deflation, eastward magma migration (leading to the distal eruption), and large eastward displacement of the eastern flank. Magma reservoir (identical to Figure 13a) is depressurized (underpressure: 10 MPa), so that the summit loads the reservoir and the eastern flank (elastoplastic edifice, $\phi = 15°$, $C = 1$ MPa). For each model, Young modulus of the edifice was 50 GPa.

previous stages (summit/proximal eruptions); by some aspects, this cycle is comparable to the one existing during stick-slip on seismic faults. If the edifice had a purely elastic rheology, the summit horizontal stress could not be relaxed and the summit eruptive system would merely lock and stop its activity.

4.3. After the Major Eruption of March–May 2007

[50] The Dolomieu crater rapid collapse on 5 April 2007 was the ultimate form of summit deflation. Substantial eastward east flank displacement and summit deflation (DERG-FERG lengthened by ~40 cm, DERG-BORG shortened by ~70 cm, Figures 6 and 7) allow the relaxation of the horizontal summit stress. FERG-DERG baseline E-W component shortens from 25 July to 4 August 2008 (Figure 6). During the August–December 2008 magma injections, only one summit station recorded a displacement greater than 2 cm (DSRG, N-S component, ~5 cm) [*Peltier et al*., 2010, Figures 6 and 7], that is, an order of magnitude lower than during 1998–2007. Note that a number of aborted intrusions, which were very rare before 2007 (Table 1) [*Peltier et al*., 2010; *Roult et al*., 2012], were observed. The rapid (hour scale), one-step, fragile rupture processes that led to the eruption type that predominated before March 2007 were replaced by the slow (month scale), incremental, plastic-type deformation as the process that transfers magma to the surface. No distal eruptions or eruptive cycles have occurred since April 2007. Notice that if there were short-term (1–3 months) magma supply rate variations from mantle at Piton de la Fournaise, they would have disappeared after April 2007. These features are coherent with a low summit horizontal stress and rock strength: A low overpressure is needed for the magma to erupt, and the subsequent erupted volume is low. As rock strength limits the maximum possible stress and maximum fluid pressure, this must be the parameter that ultimately controls the system. Threshold effects induce nonlinearity in the stress state, allowing the volcanic edifice to modulate magma transfer from a constant input rate (inferred from the inter-eruptive stages) to a discrete, cyclical production of magma quanta at the surface: The volcanic edifice acts as a valve controlling the magma production at the surface.

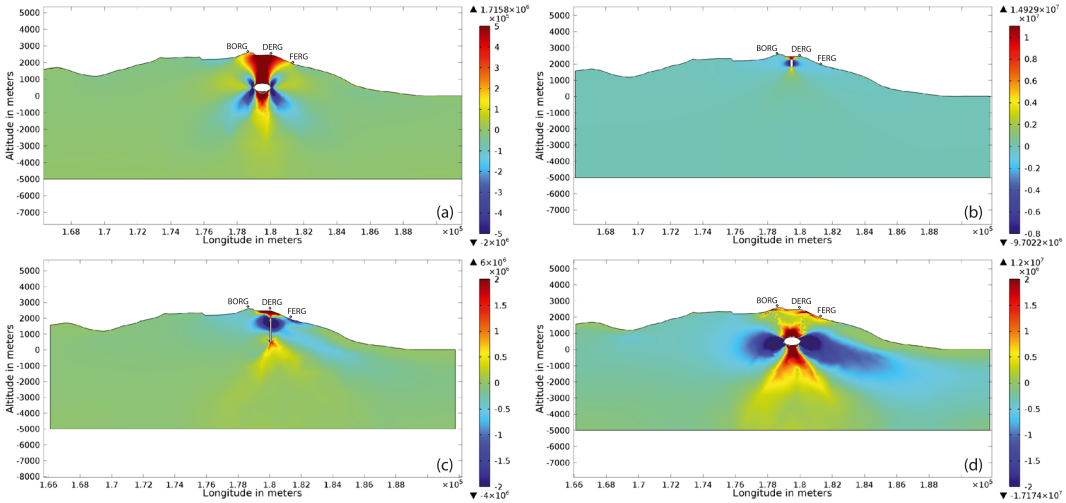

Figure 14. Horizontal stress change (color, in Pa) as a function of the longitude and altitude, for the various loading cases of the eruptive cycle presented in Figure 13. Stress is positive in tension, and negative in compression. Tension in the summit edifice, due respectively to (a) the summit inflation and (d) the eastward displacement of the eastern flank. (b) Compression in the summit edifice and (c) loading of the eastern flank. Parameters of the models are similar to Figure 13.

5. Conclusion

[51] In this paper, we used GPS data recorded from 2003 to 2009 at Piton de la Fournaise to constrain the mechanical processes that work during the eruptive cycles evidenced on this volcano. From a spatial point of view, the surface displacements exhibit a striking and strong asymmetry between the western and eastern flank of the edifice. From a temporal point of view, deformation and stresses, especially horizontal stresses, accumulate in the summit edifice during the inter-eruptive periods and summit/proximal eruptions. Distal eruptions occur when a characteristic displacement —and therefore a characteristic stress—is reached in the eastern part of the summit edifice. The distribution of the displacements recorded during eruptions in the upper eastern flank is bimodal, with small displacements occurring during summit/proximal eruptions, and large ones occurring during distal eruptions. Eruptive cycles [*Peltier et al*., 2008] comprising summit/proximal then distal eruptions have been investigated from the point of view of stress, strain, and edifice strength. Asymmetry, characteristic displacement of the eastern summit edifice, quantization of the upper east flank displacement, and eruptive cyclicity evoke a nonlinear behavior provoked by a characteristic threshold in the edifice strength, that is, an elastoplastic type rheology for the edifice. We therefore model the edifice as a homogeneous Drücker-Prager elastoplastic body submitted to stress perturbations brought by various sources. Dykes were imposed to be vertical as expected from field investigation and statistics. East-west asymmetry of the displacement during distal eruptions was well reproduced by such a homogeneous elastoplastic model, with an internal friction angle ϕ of 15° and a cohesion of 1 MPa. This computation shows that when stress (norm of the deviatoric stress tensor) reaches some threshold in the eastern flank, plastic deformation occurs and may represent a large amount of the total deformation during distal eruptions. However, fitting interdistal displacements with a low ϕ homogeneous model proved to be impossible. A model with a high ϕ ($\phi > 30°$) edifice was necessary to reproduce simultaneously the quasi-immobile flanks, the large displacements at DERG, and the E-W displacement asymmetry recorded during interdistal periods. This result shows that strain weakening occurs during the rupture of the edifice at the time of distal eruptions, allowing large plastic displacements. This strain weakening can eventually arise from the shearing of a sill structure.

[52] Such a process of plastic displacement, with stress drop in the eastern flank, relaxes the summit horizontal stress and induces reservoir depressurization, summit deflation, and finally the horizontal magma transfer up to its distal eruption. This process helps to understand the rapid stress field changes and the complex propagation of magma during distal eruptions. It also helps to understand that the eruptive cycle is a stress cycle due to the interaction of the pressurized magma with the elastoplastic edifice: Stress, especially horizontal stress, builds up slowly during inter-eruptive stages and summit/proximal eruptions to a high threshold and relaxes rapidly to a lower threshold during the plastic displacement occurring during distal eruptions. This eruptive stress cycle recalls the earthquake stress cycle.

[53] Such threshold effects therefore induce nonlinearity and periodicity in the stress state. They allow the volcanic edifice to modulate magma transfer from a constant input rate (inferred from the inter-eruptive stages) to a discrete, cyclical production of magma quanta at the surface. They favor the idea that the volcanic edifice of Piton de la Fournaise may act as a valve controlling the magma transfer from the mantle to the surface. Such an interaction between magma and edifice—a "valve effect" controlled by the edifice rheology—could be investigated on other large basaltic volcanoes where large flank movements are observed, as Kilauea [e.g., *Poland et al*., 2012; *Montgomery-Brown et al*., 2011] or Etna [e.g., *Neri et al*., 2004; *Walter et al*., 2005; *Allard et al*., 2006].

Appendix A: Estimation of the Noise at FERG on 30 March 2007, From 16:30 to 17:30

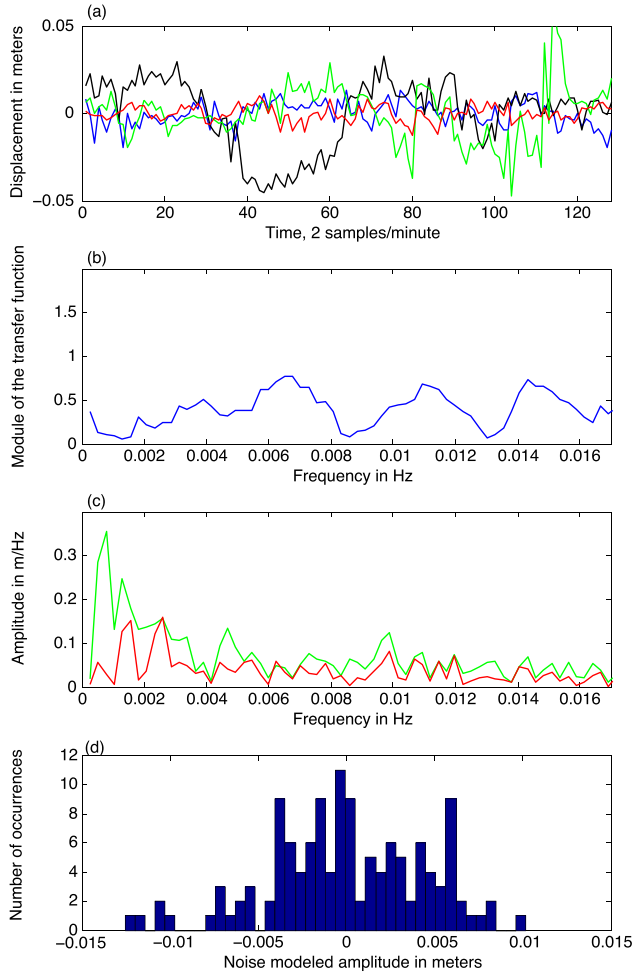

Figure A1. Estimation of the noise at FERG on 30 March 2007, from 16:30 to 17:30. (a) GPS displacement noise samples used in this estimation, as a function of time, for various GPS stations and recording time. GITG, 15:30 to 16:30 (black); FERG, 15:30 to 16:30 (blue). Both noise samples were used to compute the transfer function. GITG, 16:30 to 17:30 (filter input; green); FERG, 16:30 to 17:30 (filter output, estimated noise; red). (b) Module of the transfer function as a function of frequency, computed in the 15:30 to 16:30 time window. (c) Amplitude spectrum of the displacement noise as a function of frequency. GITG, 16:30 to 17:30 (filter input; green); FERG, 16:30 to 17:30 (filter output, estimated noise; red). (d) Histogram showing the sample probability density function of the noise estimated at FERG from 16:30 to 17:30.

[54] **Acknowledgments.** Part of this work was supported by the Agence Nationale de la Recherche under contract ANR-08-RISK-011 (UnderVolc) and the EMERGENCE–Ville De Paris project. This is IPGP contribution 3425.

References

Allard, P., B. Behncke, S. d'Amico, M. Neri, and S. Gambino (2006), Mount Etna 1993–2005: Anatomy of an evolving eruptive cycle, *Earth Sci. Rev.*, *78*, 85–114.

Augier, A. (2011), Etude de l'éruption d'Avril 2007 du Piton de la Fournaise (île de la Réunion) à partir de données d'interférométrie RADAR et GPS, développement et application de procédures de modélisation, Thèse, 300 p., Université de Clermont-Ferrand.

Augier, A., et al. (2008), The April 2007 eruption at Piton de la Fournaise, Réunion Island, imaged with ENVISAT-ASAR and ALOS-PALSAR data, USEReST workshop, Napoli, Italy.

Bachèlery, P. (1981), Le Piton de la Fournaise (île de la Réunion). Etude volcanologique structurale, Thèse, Université de Clermont-Ferrand.

Behncke, B., and M. Neri (2003), Cycles and trends in the recent eruptive behaviour of Mount Etna (Italy), *Can. J. Earth Sci.*, *40*, 1405–1411, doi:10.1139/E03-052.

Bonali, F. L., C. Corazzato, and A. Tibaldi (2010), Identifying rift zones on volcanoes: An example from La Réunion Island, Indian Ocean, *Bull. Volcanol.*, doi:10.1007/s00445-010-0416-1.

Brooks, B. A., J. H. Foster, M. Bevis, L. N. Frazer, C. J. Wolfe, and M. Behn (2006), Periodic slow earthquakes on the flank of Kilauea Volcano, Hawai'i, *Earth Planet. Sci. Lett.*, *246*, 207–216, doi:10.1016/j.epsl.2006.03.035.

Brooks, B. A., J. H. Foster, D. Sandwell, C. J. Wolfe, P. G. Okubo, M. Poland, and D. Myer (2008), Magmatically triggered slow slip at Kilauea Volcano, Hawaii, *Science*, *321*, 1177, doi:10.1126/science.1159,007.

Cervelli, P., P. Segall, K. Johnson, M. Lisowski, and A. Miklius (2002), Sudden aseismic fault slip on the south flank of Kilauea volcano, *Nature*, *415*, 1014–1018, doi:10.1038/4151014a.

Clarke, D., F. Brenguier, J.-L. Froger, N. Shapiro, A. Peltier, and T. Staudacher (2013), Timing of a large volcanic movement at Piton de la Fournaise volcano using noise-based seismic monitoring and ground deformation measurements, *Geophys. J. Int.*, doi:10.1093/gji/ggt276.

Collombet, M., J.-R. Grasso, and V. Ferrazzini (2003), Seismicity rate before eruptions on Piton de la Fournaise volcano: Implications for eruption dynamics, *Geophys. Res. Lett.*, *30*(21), 2099, doi:10.1029/2003GL017494.

Drücker, D. C., and W. Prager (1952), Soil mechanics and plastic analysis or limit design, *Q. Appl. Math.*, *10*, 157–165.

Famin, V., and L. Michon (2010), Volcano destabilization by magma injection in a detachment, *Geology*, *38*, 219–222.

Famin, V., B. Welsch, S. Okumura, P. Bachèlery, and S. Nakashima (2009), Three differentiation stages of a single magma at Piton de la Fournaise (Réunion hotspot), *G-Cubed*, *10*(1), Q01007, doi:10.1029/2008GC00201.

Fukushima, Y., V. Cayol, and P. Durand (2005), Finding realistic dike models from interferometric synthetic aperture radar data: The February 2000 eruption at Piton de la Fournaise, *J. Geophys. Res.*, *110*, B03206, doi:10.1029/2004JB003268.

Kachanov, L. M. (1958), On creep rupture time, *Izv. Acad. Nauk. SSSR, Otd. Tekh. Nauk.*, *8*, 26–31.

Letourneur, L., A. Peltier, T. Staudacher, and A. Gudmundsson (2008), The effects of rock heterogeneities on dyke paths and asymmetric ground deformation: The example of Piton de la Fournaise (Réunion Island), *J. Volcanol. Geotherm. Res.*, *173*(3–4), 289–302.

Michon, L., F. Saint-Ange, P. Bachèlery, N. Villeneuve, and T. Staudacher (2007a), Role of the structural inheritance of the oceanic lithosphere in the magmato-tectonic evolution of Piton de la Fournaise volcano (La Réunion Island), *J. Geophys. Res.*, *112*, B04205, doi:10.1029/2006JB004598.

Michon, L., T. Staudacher, V. Ferrazzini, P. Bachèlery, and J. Marti (2007b), April 2007 collapse of Piton de La Fournaise: A new example of caldera formation, *Geophys. Res. Lett.*, *34*, L21301, doi:10.1029/2007GL031248.

Michon, L., V. Cayol, L. Letourneur, A. Peltier, N. Villeneuve, and T. Staudacher (2009), Edifice growth, deformation and rift zone development in basaltic setting: Insight from Piton de la Fournaise shield volcano (Réunion Island), *J. Volcanol. Geotherm. Res.*, *184*, 14–30, doi:10.1016/j.jvolgeores.2008.11.002.

Montgomery-Brown, E. K., D. K. Sinnett, K. M. Larson, M. P. Poland, P. Segall, and A. Miklius (2011), Spatiotemporal evolution of dike opening and décollement slip at Kīlauea Volcano, Hawai'i, *J. Geophys. Res.*, *116*, B03401, doi:10.1029/2010JB007762.

Nercessian, A., A. Hirn, J.-C. Lépine, and M. Sapin (1996), Internal structure of Piton de la Fournaise volcano from seismic wave propagation and earthquake distribution, *J. Volcanol. Geotherm. Res.*, *184*, 123–143.

Neri, M., V. Acocella, and B. Behncke (2004), The role of the Pernicana Fault System in the spreading of Mt. Etna (Italy) during the 2002–2003 eruption, *Bull. Volcanol.*, *66*, 417–430.

Norini, G., and V. Acocella (2011), Analogue modelling of flank instability at Mount Etna: Understanding the driving factors, *J. Geophys. Res.*, *116*, B07206, doi:10.1029/2011JB008216.

Owen, S., P. Segall, J. Freymueller, A. Miklius, R. Denlinger, T. Arnadottir, M. Sako, and R. Bürgmann (1995), Rapid deformation of the South Flank of Kilauea Volcano, Hawaii, *Science*, *267*, 5205, 1328–1332.

Peltier, A., T. Staudacher, and P. Bachèlery (2007), Constraints on magma transfers and structures involved in the 2003 activity at Piton de La Fournaise from displacement data, *J. Geophys. Res.*, *112*, B03207, doi:10.1029/2006JB004379.

Peltier, A., V. Famin, P. Bachèlery, V. Cayol, Y. Fukushima, and T. Staudacher (2008), Cyclic magma storages and transfers at Piton de La Fournaise volcano (La Réunion hotspot) inferred from deformation and geochemical data, *Earth Planet. Sci. Lett.*, *270*(3–4), 180–188.

Peltier, A., P. Bachèlery, and T. Staudacher (2009a), Magma transfer and storage at Piton de la Fournaise (La Réunion Island) between 1972 and 2007: A review of geophysical and geochemical data, *J. Volcanol. Geotherm. Res.*, *184*(1–2), 93–108.

Peltier, A., T. Staudacher, P. Bachèlery, and V. Cayol (2009b), Formation of the April 2007 caldera collapse at Piton de La Fournaise volcano: Insights from GPS data, *J. Volcanol. Geotherm. Res.*, *184*(1–2), 152–163.

Peltier, A., T. Staudacher, and P. Bachèlery (2010), New behaviour of the Piton de La Fournaise volcano feeding system (La Réunion Island deduced from GPS data: Influence of the 2007 Dolomieu crater collapse, *J. Volcanol. Geotherm. Res.*, *192*, 48–56.

Peltier, A., F. Massin, P. Bachèlery, and A. Finizola (2012), Internal structure and building of basaltic shield volcanoes: The example of the Piton de la Fournaise terminal cone (La Réunion), *Bull. Volcanol.*, *74*, 1881–1897.

Poland, M. P., A. Miklius, A. J. Sutton, and C. R. Thornber (2012), A mantle-driven surge in magma supply to Kilauea Volcano during 2003–2007, *Nat. Geosci.*, *5*, 295–300, doi:10.1038/NGEO1426.

Prono, E., V. Monteiller, J. Battaglia, J.-L. Got, and V. Ferrazzini (2009), 3D P-wave travel-time tomography of Le Piton de la Fournaise volcano, La Réunion (France), from 1996–1999 earthquake data, *J. Volcanol. Geotherm. Res.*, doi:10.1016/j.volgeores.2008.12.009.

Roult, G., A. Peltier, B. Taisne, T. Staudacher, V. Ferrazini, and A. di Muro (2012), A new comprehensive classification of the Piton de la Fournaise activity spanning the 1985–2010 period. Search and analysis of short-term precursors from a broad-band seismological station, *J. Volcanol. Geotherm. Res.*, doi:10.1016/j.volgeores.2012.06.012.

Schiffman, P., R. J. Watters, N. Thompson, and A. W. Walton (2006), Hyaloclastites and the slope stability of Hawaiian volcanoes: Insights from the Hawaiian Scientific Drilling Project's 3-km drill core, *J. Volcanol. Geotherm. Res.*, *151*, 217–228.

Schmid, A., J.-R. Grasso, D. Clarke, V. Ferrazzini, P. Bachèlery, and T. Staudacher (2012), Eruption forerunners from multi-parameter monitoring and application for predictability, *J. Geophys. Res.*, *117*, B11203, doi:10.1029/2012JB009167.

Segall, P., E. Desmarais, A. Shelly, A. Miklius, and P. Cervelli (2006), Earthquakes triggered by silent slip events on Kilauea volcano, Hawaii, *Nature*, *442*, 71–74, doi:10.1038/nature04938.

Staudacher, T., V. Ferrazzini, A. Peltier, P. Kowalski, P. Boissier, P. Catherine, F. Lauret, and F. Massin (2009), The April 2007 eruption and the Dolomieu crater collapse, two major events at Piton de la Fournaise, *J. Volcanol. Geotherm. Res.*, *184*(1–2), 126–137.

Swanson, D. A., W. A. Duffield, and R. S. Fiske (1976), Displacement of the south flank of Kilauea volcano: The result of forceful intrusion of magma into the rift zones, *U.S. Geol. Surv. Prof. Pap.*, *963*, 1–39.

Tinard, P. (2007), Caractérisation et modélisation des déplacements du sol associés à l'activité volcanique du Piton de la Fournaise, île de la Réunion, à partir de données interférométriques, Thèse, 334 p., Université de Clermont-Ferrand.

Valko, P., and M. J. Ekonomides (2001), *Hydraulic Fracture Mechanics*, p. 298, John Wiley & Sons Ltd., Chichester, U.K.

Vidal, V., and A. Bonneville (2004), Variations of the Hawaiian hot spot activity revealed by variations in the magma production rate, *J. Geophys. Res.*, *109*, doi:10.1029/2003JB002559.

Walter, T., V. Acocella, M. Neri, and F. Amelung (2005), Feedback processes between magmatic events and flank movement at Mount Etna (Italy) during the 2002–2003 eruption, *J. Geophys. Res.*, *110*, B10205, doi:10.1029/2005JB003688.